

ARTICLE

<https://doi.org/10.1038/s42004-018-0097-9>

OPEN

Air-stable phosphorus-doped molybdenum nitride for enhanced electrocatalytic hydrogen evolution

Junqing Yan¹, Lingqiao Kong¹, Yujin Ji², Youyong Li², Jai White³, Shengzhong (Frank) Liu^{1,4}, Xiaopeng Han⁵, Shuit-Tong Lee² & Tianyi Ma³

Molybdenum-based electrocatalysts for hydrogen evolution have been investigated extensively in recent years. However, unlike other non-oxides, molybdenum nitride generally shows a weak preference for hydrogen evolution and low performance owing to surface oxidation and the strong Mo–H bond. Here, we prepare an air-stable molybdenum nitride through a multi-step solid-state reaction. We find that a uniformly dispersed mixture of the precursors is optimal for preparation of the electrocatalyst. To further enhance hydrogen evolution performance towards practical device applications, phosphorus doping is carried out, using a few layered black phosphorus source. The phosphorus-doped molybdenum nitride (P–Mo–N) sample catalyzes hydrogen evolution with potentials of 105, 145, and 157 mV at the current densities of 10, 50, and 100 mA/cm², respectively, in 0.5 M H₂SO₄ solution with a small Tafel slope of 43 mV/dec. Thus it outperforms many of the state-of-art molybdenum-based hydrogen evolution catalysts reported to date.

¹Key Laboratory of Applied Surface and Colloid Chemistry, Ministry of Education, Shaanxi Key Laboratory for Advanced Energy Devices, Shaanxi Engineering Lab for Advanced Energy Technology, School of Materials Science and Engineering, Shaanxi Normal University, Xi'an 710119, People's Republic of China.

²Institute of Functional Nano and Soft Materials (FUNSOM), Jiangsu Key Laboratory for Carbon-Based Functional Materials and Devices, Soochow University, Suzhou, Jiangsu 215123, People's Republic of China. ³Discipline of Chemistry, School of Environmental and Life Sciences, University of Newcastle, Callaghan, NSW, Australia. ⁴iChEM, Dalian Institute of Chemical Physics, Dalian National Laboratory for Clean Energy, Chinese Academy of Sciences, Dalian 116023, People's Republic of China. ⁵School of Materials Science and Engineering, Tianjin Key Laboratory of Composite and Functional Materials, Tianjin University, Tianjin 300072, China. These authors contributed equally: Junqing Yan, Lingqiao Kong, Yujin Ji. Correspondence and requests for materials should be addressed to Y.L. (email: yyli@suda.edu.cn) or to S.L. (email: liusz@snnu.edu.cn) or to T.M. (email: tianyi.ma@newcastle.edu.au)

Hydrogen evolution reaction (HER) from electrocatalytic water splitting has been regarded as one of the important strategies to solve the world's increasing energy and environment issues^{1–10}. Water electrolysis requires a stable electrocatalyst which has the ability to overcome high overpotential and provide efficient activity. To date, Pt-group materials are still the most commonly used catalysts in the commercial HER and there is a demand for a necessary replacement due to their limited supply and high cost^{11–20}. For the sustainable and large-scale application of HER, earth-abundant materials have been under intense investigation in an effort to reach a suitable Pt-like HER performance^{21–30}. For the typical HER process, two accepted reaction mechanisms are described, namely the Volmer–Heyrovsky route and Volmer–Tafel route^{31–34}. In the Volmer reaction, the formation of M–H takes place by proton adsorption on the surface sites of the catalyst. In the subsequent Heyrovsky reaction, one M–H undergoes proton-coupled electron transfer reaction to release one H₂. Whereas, for the Tafel step, two nearby adsorbed *H (H–M) combine into one H₂. Based on the abundant research in recent years, a good Pt-like HER catalyst in acidic solution should exhibit suitable proton adsorption ability and a fast carrier migration^{21–30}.

Mo-based materials are widely explored for improved HER performance^{21–25,35–40}. In particular, undoped Mo₂N has a metallic electronic structure and an excellent Pt/Pd-like hydrogenation ability. Undoped Mo₂N are frequently used in HER, but exhibits moderate performance in comparison with Mo₂C or MoP^{41–43}. This is caused by the high electronegativity of N species, which can induce a strong Mo–H bond and then weaken the H₂ generation rate⁴⁰. To improve the electrocatalytic performance, doping strategies have been widely used^{44–51}. The most significant advantage of doping has been to obtain a suitable M–H bond with moderate strength^{44,46,50,51}. Moreover, N doping is reported to improve the electrocatalytic hydrogen performance of MoP by reducing the electrical resistance, increasing the number and quality of active sites⁵². The non-metal constituents, nitrogen (N) and phosphorous (P) belong to the same group family and thus have a similar electronic structure. However, phosphorus is more electronegative (2.19) than nitrogen (3.04), and thus, the replacement of N by P may lead to a weakened M–H bond^{50,51}. However, thus far, P-doped molybdenum nitride for improving HER performance has not been studied in detail.

One key challenge for obtaining a high HER activity is to locate the electroactive sites of catalysts. The edge sites exposed doped elements or vacancies are reported to be responsible for the enhanced reaction performance^{50–55}. Increasing the number of reaction sites has been one major explored strategy. For the synthesis of Mo₂N, ammonia reduction of molybdenum oxide is widely used through high-temperature calcination, which could induce the expected aggregation, thus reducing the exposed reaction sites and weakening the corresponding electrocatalytic activity. However, the releasing of the in situ generated gas can promote the formation of holes or disordered lattice structures, thereby avoiding the aggregation and increasing active sites^{53,55}.

Herein, we report a two-step synthesis strategy to prepare P-doped Mo₂N. The mixture of MoO₃ and ethanediamine are first treated by high-strength solid-phase grinding and then calcinated in an N₂ atmosphere. Mo₂N is obtained with abundant exposed grain-boundary sites (Mo–N). Few layered black phosphorus (BP) is used for P doping via vacuum stirring of the BP and Mo₂N mixture, followed by calcination to obtain P–Mo₂N (P–Mo–N). The obtained samples of Mo–N and P–Mo–N display notable electrocatalytic HER performance and stability, even at a high current density of 160 mA/cm².

Results

Synthesis of Mo–N and P–Mo–N. First, Mo₂N (Mo₂N-r) was synthesized from the reduction reaction of MoO₃ by the release of

in situ NH₃ similar to previous work conducted using melamine as the NH₃ source³⁹. Solid-state reaction has been used previously to generate samples with numerous holes and vacancies due to the in situ release of gases^{53,55}. Owing to its active character, Mo₂N can be oxidized easily at ambient conditions. Supplementary Figure 1a shows the photograph of the autoignition of Mo₂N-r. Such an active material owns so many surface oxidation states that its catalytic activity is relatively low^{41–43}. More exposed Mo sites may be responsible for the above active phenomenon of autoignition. To obtain a relatively stable sample, ethanediamine was used to generate in situ NH₃. This was also expected to change the crystal faces via the release of gases during its decomposition. The layered MoO₃ and ethanediamine (mass ratio: 1:2) were mixed thoroughly by a ball grinder (Fig. 1a). The mixture was then calcined in an N₂ atmosphere. After that, a layered graphite-like sample (Mo–N-2) without autoignition characteristics was obtained as shown in Supplementary Figure 1b. The crystal structure was confirmed to be Mo₂N from the X-ray diffraction (XRD) measurement (Supplementary Figure 1c). The direct appearance of the two samples was tested by scanning electron microscopy (SEM). As shown in Supplementary Figure 2, Mo₂N-r and Mo–N-2 give the aggregated and layered structures, respectively. The samples from the two different processes were measured by transmission electron microscope (TEM) to further check their morphologies. Mo₂N-r and Mo–N-2 both show the layered structure; however, the ethanediamine-induced sample presents some obvious particles (Supplementary Figure 3). The high resolution TEM in Supplementary Figure 4 shows the detailed difference of the two samples. Mo₂N-r shows the typical continuous lattice structure while Mo–N-2 gives obvious crossed lattice fringes, that is, for the Mo–N-2 sample, the formed nanoparticles combine together to maintain the apparent nanosheet morphology (Supplementary Figure 2). This suggests that the ethanediamine-based solid-state reaction can induce the dismemberment of layered MoO₃ to form nanoparticles, and then generate more grain-boundaries under the releasing of gases. To get the suitable grain-boundary and prevent aggregation, the amount of ethanediamine was tested. The mass ratios of MoO₃ to ethanediamine were increased from 1:3 to 1:4 to 1:5. Supplementary Figure 5 shows the corresponding XRD results of obtained samples (Mo–N-n). Only the Mo₂N phase can be found in three samples indicating no noticeable change to the crystal lattice structure even at the highest ratios (Supplementary Figure 5a). The TEM images show obvious grain-boundaries, as well as some detectable lattice distortion (Supplementary Figure 5b–d). Please note that all the synthesized samples of Mo–N-x present the appearance of nanosheet, which is composed of nanoparticles.

The electrocatalytic hydrogen generation from water splitting in 0.5 M H₂SO₄ solution was carried out for detecting the activity of the obtained samples. The Mo–N-n samples give an enhanced HER performance obviously compared with Mo₂N-r (Supplementary Figure 6), suggesting that the ethanediamine-driven Mo₂N samples have a dominant Mo–H adsorption–desorption performance. More grain-boundary sites, i.e. more nanoparticle formation from the sufficient reduction reaction between ethanediamine and MoO₃ is the internal origin^{53,55}. With increasing ethanediamine content, the HER performance increases accordingly. For the samples obtained from MoO₃ and ethanediamine mass ratio: 1:4 and 1:5 (Mo–N-4 and Mo–N-5) show a similar activity. Therefore, Mo–N-4 (Mo–N) was selected for further research.

At the second step, P doping was carried out to further modulate their HER performance as show in Fig. 1b–d. The Mo–N sample and layered black phosphorus (BP)^{56,57} were used as the precursors. Few layered BP is not stable in air and can be oxidized to PO_x species, which can be reduced and doped into Mo₂N lattices. Moreover, few-layer BPs still keep the structural

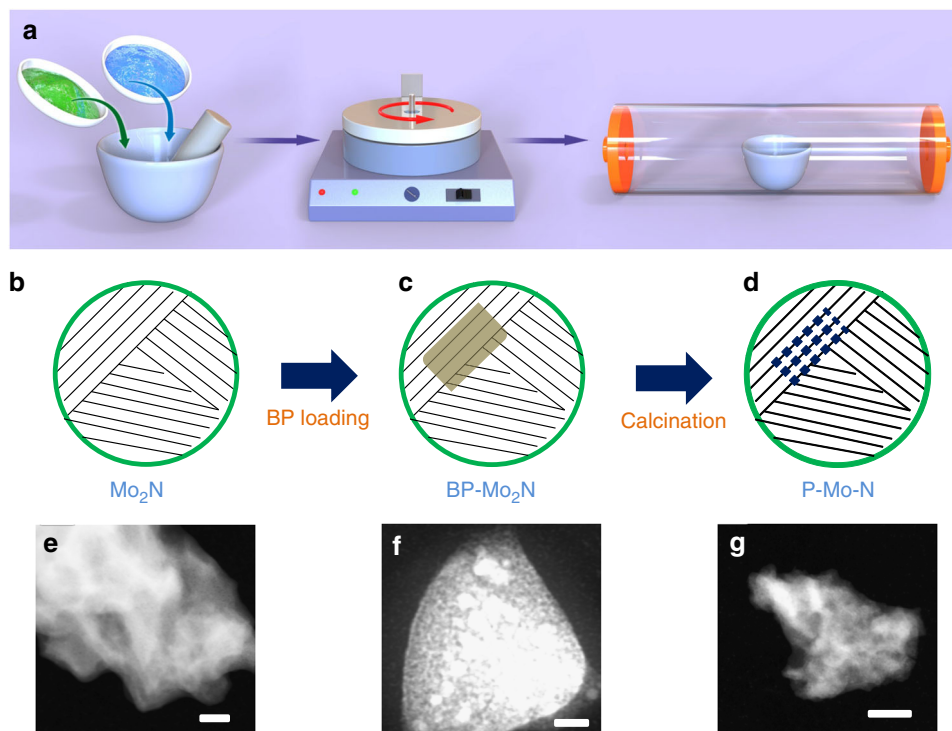


Fig. 1 Synthesis of Mo_2N and $\text{P-Mo}_2\text{N}$. **a** Schematic illustration of the synthesis of Mo_2N , two precursors in **a** are ethanediamine and MoO_3 , respectively. **b** The surface model of Mo_2N , which is used for BP loading, that is, BP and Mo_2N are treated by vacuum stirring. **c** The surface model of $\text{BP-Mo}_2\text{N}$, the gray part is loaded BP. **d** The model of P doped Mo_2N lattice structure, the blue dots are P element in the lattice. **e-g** The corresponding TEM images of Mo_2N , $\text{BP-Mo}_2\text{N}$, and $\text{P-Mo}_2\text{N}$, respectively. The scale bars are 50, 20, and 50 nm in **e**, **f**, and **g**, respectively. The white spots in TEM image of $\text{BP-Mo}_2\text{N}$ is the BP, which disappears after the calcination treatment as shown in $\text{P-Mo}_2\text{N}$ image, suggesting the P doping into the lattice of Mo_2N

integrity of Mo_2N during the P doping process. Supplementary Figure 7 shows the typical TEM images of BP, the layered structure can be detected. The mixture of the Mo-N sample and BP was collected after about 3 h vacuum-stirring with the BP being loaded onto the surface of Mo-N (Fig. 1c). After storage in air for 1 day, the sample was treated by calcination with the adding of ethanediamine in an N_2 atmosphere to finalize the P doping (Fig. 1d). Figure 1 also shows the corresponding TEM images of the Mo-N samples. Clearly, the image of the P doped sample (Supplementary Figure 8) shows a disordered lattice structure, because of the large ionic radius of P. To confirm the negligible impact of secondary calcination on the HER performance, the reference sample without BP addition was synthesized. As given in Supplementary Figure 9, the XRD pattern does not show an obvious change compared with the initial one (Supplementary Figure 9a). The HER activity also remains unchanged (Supplementary Figure 9b). The obtained sample was named as P-Mo-N for the following discussion, in which the P content was 10 wt.% (Please note that the P content of P-Mo-N samples was detected by X-ray photoelectron spectroscopy (XPS) measurements and is semi-quantitative). The specific surface areas of the samples were further measured by N_2 adsorption-desorption method, calculated by multiple spot Brunauer-Emmett-Teller (BET) theory. As shown in Supplementary Figure 10, the BET surface areas of $\text{Mo}_2\text{N-r}$, Mo-N , and P-Mo-N are 4.48, 5.54, and 5.38 m^2/g , respectively, further confirming that the ethanediamine-driven method can avoid the aggregation.

Characterization of P-Mo-N . Figure 2a shows the XRD pattern of P-Mo-N sample, four typical peaks are located at 2 theta of 37°, 41°, 62°, and 74.5°, which can be attributed to (112), (200), (220), and (312) of tetragonal Mo_2N (PDF: 25-1368). Compared

with the initial Mo-N sample, no obvious change of peak position and intensity suggests that the secondary calcination of P doping hardly changes the crystalline structure. From the SEM images in Fig. 2b and Supplementary Figure 11, the Mo-N and P-Mo-N samples give a nanosheet-like appearance (Supplementary Figure 11a–b). In the magnified SEM in Fig. 2b and Supplementary Figure 11c, nanoparticles with a size of ca. 8 nm can be found, evidencing that the rough nanosheets of Mo-N and P-Mo-N samples are formed by nano-sized particles. The TEM image of P-Mo-N was shown in Fig. 2c. Clearly, the nanoparticles can be found along the nanosheet edge. The inset shows the corresponding electron diffraction spectrum (EDS), revealing the typical four crystal faces, which is consistent with the XRD pattern (Fig. 2a). We also presented the TEM images of the reference P-Mo-N samples with 9.5 wt.% and 10.5 wt.% P doping. As shown in Supplementary Figure 12, TEM images similar to that of the 10 wt.% sample P-Mo-N can be found, with both of them giving the rough sheet surface. The corresponding EDS results suggest that the Mo_2N phase was obtained and the P content in this range hardly affects the final product formation. The HRTEM image of the P-Mo-N sample in Fig. 2d further suggests the existence of nanoparticles. The obvious grain boundaries can be found and two interplanar crystal spacing values are measured to be 0.24 and 0.21 nm, which can be assigned to the (112) and (200) crystal faces, respectively. The disordered lattice fringes can also be detected. Supplementary Figure 13 gives the corresponding HRTEM images of the reference P doped samples with similar results. Figure 2e gives the element mapping result of P-Mo-N sample. Clearly, the elements of Mo, N, and P show uniform distribution. We also give the element mapping of the reference sample of Mo-N as shown in Supplementary Figure 14, only two elements of Mo and N can be detected.

XPS was further carried out for obtaining more information about the surface and sub-surface states. In the Mo 3d region for

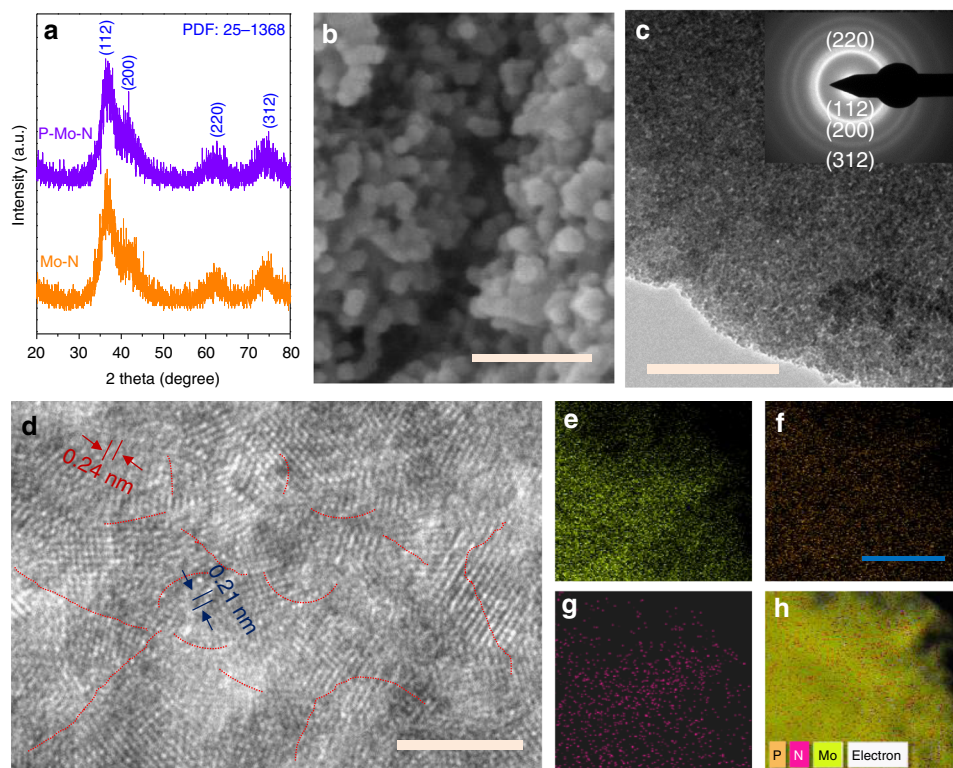


Fig. 2 Physical characterization of P-Mo-N. **a** XRD pattern of the Mo-N and P-Mo-N, the PDF number (25-1368) of standard Mo₂N is shown. **b** SEM image of P-Mo-N sample, scale bar: 50 nm. **c** TEM image of P-Mo-N, the scale bar is 50 nm, the inset shows the corresponding EDS result with the crystal indices. **d** HRTEM image of P-Mo-N, the obvious grain-boundaries are marked by red dots, two interplanar spacing values of 0.24 and 0.21 nm are also shown, scale bar: 1 nm; The element mapping of P-Mo-N sample, **e** Mo element, **f** N element, **g** P element, and **h** the mixed result, scale bar: 50 nm

the Mo-N and P-Mo-N as shown in Supplementary Figure 15a, for the Mo-N sample, the Mo 3d core level spectrum can be fitted into four peaks, i.e. two pairs of 229.2 and 232.2 eV, 233.2, and 236.2 eV. The first pair is attributed to Mo-N bonds, in which the high binding energy value is ascribed to MoO₃⁵⁸, and the existence of oxide suggests the oxidization of the surface Mo species. For the P doped Mo₂N, a pair of new peaks located at 230.1 and 232.7 eV can be detected and can be assigned to the Mo-P peaks^{59,60}, confirming that the P has been doped into the Mo₂N lattice. Moreover, the positions of Mo 3d peaks for Mo-N and Mo-O bonds show a slight shift towards the low binding energy region as shown in Supplementary Table 1. This phenomenon may originate from the P doping that can share the Mo binding bond and then weaken their bonding energy. Note that the full width at half maximum of the Mo-N bonds for the two samples of Mo-N and P-Mo-N is the same (1 eV), further suggesting the formation of the Mo-P bond after P doping. For N 1s XPS spectrum in Supplementary Figure 15b, two main peaks can be found for both Mo-N and P-Mo-N. The first peak located at 395.1 eV belongs to the Mo 3p core level, and the second peak at 398.3 eV is attributable to Mo-N bond. For P-Mo-N, the N 1s peak gives a noticeable shift to 398.26 eV (398.3 eV of bare Mo-N), suggesting that the P element has been doped into the Mo₂N lattice by replacing one N element. For the P 2p XPS spectrum of P-Mo-N in Supplementary Figure 15c, one main peak can be fitted into two peaks, located at 130.1 and 131.2 eV. This low binding energy peak can be assigned to the Mo-P bond. Furthermore, 1 weak peak at ca. 133.6 eV attributable to PO_x can also be detected. The BP was reduced by urea during the calcination and then most of the elemental P was in situ doped into the lattice of formed Mo₂N. To confirm the above assumption, two steps of P doping process were picked out for

checking the change of Mo, N, and P valence states. The first step was the original sample i.e. PO_x/Mo₂N; this sample was treated about 1 h with the existence of urea and N₂ and denoted as PO_x/P-Mo₂N. Supplementary Figure 16 shows the corresponding XPS results. For the Mo 3d XPS spectrum (Supplementary Figure 16a), like the pure Mo₂N, the sample of PO_x/Mo₂N shows the typical four peaks attributable to the Mo-N and Mo-O (MoO₃) bonds. However, the PO_x/P-Mo₂N sample, which is not a completely reduced sample, shows a different result compared with the initial sample. At the binding energy of ca. 230.0 and 232.6 eV, two weak peaks, which can be assigned to the formation of MoP_x, are found, suggesting that a proportion of the used P has been doped into the Mo₂N lattice. For the N 1s XPS spectra, the similar results compared with the patterns in Supplementary Figure 16b can be found. However, the N 1s binding energy of PO_x/P-Mo₂N sample is ca. 298.28 eV, slightly smaller than that of PO_x/Mo₂N (398.3 eV) and higher than that of P-Mo-N (398.26 eV), further confirming the successful P doping into the Mo₂N lattice. For the P 2p XPS spectrum in Supplementary Figure 16c, the sample of PO_x/Mo₂N exhibits a strong peak located at 133.7 eV, which comes from the surface of PO_x species. Meanwhile, for PO_x/P-Mo₂N, the peak centered at 133.7 eV is weakened and two new peaks (130.0 and 131.1 eV) appear, suggesting the doped P element exists at the low valence state. Based on the above analysis, Supplementary Figure 16d gives the models of the P doping process: at the first stage, the PO_x species is only adsorbed onto the surface of Mo₂N; during calcination, the P element of PO_x will be reduced into the low valence P and doped into the lattice of Mo₂N; after the calcination (2 h), all the P was reduced and in situ incorporated into the Mo₂N phase.

As discussed earlier, to further confirm the present samples are not formed by simple physical aggregation, the Mo-N and

P–Mo–N were treated by 12 h ultrasound. After the centrifugation, the supernate was chosen for the TEM measurement. As shown in Supplementary Figure 17, the two samples both show unchanged morphology. The crystal boundaries can be still found, suggesting that the different nanoparticles are fastened together with each other strongly, not a physical mixture. During the synthesis process, the ethanediamine and MoO₃ were grinded thoroughly and then a uniform mixture was obtained. Under the calcination, ethanediamine released NH₃ and other gases, which reacted with MoO₃ to form Mo₂N. During the reaction, the layered structure of MoO₃ was destroyed with the formation of Mo₂N nanoparticles. The calcination further combined the particles with many crystal boundaries with the disordered crystal lattices obtained. To the best of our knowledge, it is the first time to report one stable Mo₂N sample in air, and the exposed different crystal surfaces may be responsible for the above novel phenomena i.e. air-stable and high HER performance.

HER performance of Mo–N and P–Mo–N. Most of electrocatalytic HER among Mo-based samples reported to date investigate their carbides or phosphates in acidic media. Owing to the relative strong electronegativity of N, the molybdenum nitride samples exhibited a low activity^{37,39}. Herein, the capability of HER electrocatalysis of P–Mo–N sample was explored in 0.5 M H₂SO₄ solution at ambient temperature. The samples were prepared into a homogeneous ink with Nafion solution and isopropanol and then dropped onto the glassy carbon electrodes for the HER measurements. The potentials obtained from the measurements were converted to values relative to a reversible hydrogen electrode (RHE). Figure 3a shows the relevant polarization curves of different electrodes, including P–Mo–N and the reference samples of Mo₂N-r and Mo–N. The purchased 20% Pt/C electrode was also used as a standard sample. Obviously, the activity trend is as follows: Mo₂N-r < Mo–N < P–Mo–N < Pt/C, with the onset potentials (defined as the overpotential at current density of -1 mA cm^{-2}) of 74, 73, 28, and 17 mV, respectively. Moreover, compared to the reference Mo₂N-r and Mo–N, the P doped sample presents a sharply enhanced current response at low applied potentials, suggesting that the P doping can boost a better proton transfer and adsorption–desorption processes. Then the potentials at four current density values of 10, 50, 100, and 150 mA/cm² were compared as shown in Fig. 3b. Mo₂N-r and Mo–N both present relatively high potentials, larger than 200 mV. For the P doped Mo₂N, a sharp decrease can be detected in comparison to the two undoped samples. In details, the P–Mo–N sample gives the potentials of 105, 145, 157, and 164 mV at 10, 50, 100, and 150 mA/cm², respectively. As a contrast, the Pt/C sample exhibits a potential of 47 mV at the 10 mA/cm² condition, similar to the reported values in the literature^{8,42,44}. Figure 3c gives the corresponding Tafel slope results of the samples under study. The referenced commercial Pt/C sample gives the smallest slope of 37 mV/dec, followed by P–Mo–N of 43 mV/dec, Mo–N of 76 mV/dec, and Mo₂N-r of 71 mV/dec. A slope larger than 30 mV/dec for the P–Mo–N sample suggests a Volmer–Heyrovsky route for HER^{10,11,14}. The exchange current density (j_0), the most inherent measure of HER activity, was also calculated based on the Tafel equations (Supplementary Table 2). The j_0 values of P–Mo–N, Mo–N and Mo₂N-r are 0.02, 0.0052, and $6.67 \times 10^{-6} \text{ mA/cm}^2$, respectively. The P doping can facilitate a large exchange current density, increasing by a factor of 4 in comparison with the undoped samples. Supplementary Table 3 gives the direct activity comparison of P–Mo–N with the Mo-based samples recently reported in the literature. Obviously, our P–Mo–N sample gave the best HER performance in 0.5 M H₂SO₄ solution in terms of current density and Tafel slope. To further confirm the reaction sites to be the P sites on the surface of Mo₂N, the MoP and N doped MoP were also synthesized⁵².

Supplementary Figure 18a gave the XRD patterns of MoP (PDF: 24-0771) and Supplementary Figure 18b showed the corresponding HER performance. Clearly, although Mo₂N shows the lowest HER activity, the P doped Mo₂N gives the best.

The electrochemical impedance spectroscopy (EIS) was carried out to probe charge transfer processes on the catalysts in 0.5 M H₂SO₄ solution. Figure 3d shows the Nyquist plots of the samples of Mo₂N-r, Mo–N and P–Mo–N under a 250 mV potential condition. Clearly, the P doped sample gives the smallest circular arc, followed by Mo–N, Mo₂N-r, suggesting that the P–Mo–N has a relative small carrier migration resistance. Supplementary Figure 19 shows the Nyquist plot of reference Pt/C sample and the corresponding fitted circuit diagram. The R_{Ω} and R_{ct} mean the electrode resistance and carrier transfer resistance across the catalyst/solution interface, respectively. The Warburg and CPE are diffusion resistance and the constant phase element, both are out of consideration owing to the limited applying frequency in our present work. Supplementary Table 4 shows the corresponding fitted results of R_{Ω} and R_{ct} of the three samples. Typically, all the samples give a similar R_{Ω} value (0.15 ohm), suggesting the resistance of catalyst/electrode is almost the same. Regarding R_{ct} , the three samples of Mo₂N-r, Mo–N and P–Mo–N give decreased values from 111.2, to 50.02 to 14.69 ohm, respectively, confirming that the P doping can induce a suitable proton adsorption–desorption, and then decrease the resistance of the solid/solution interface. To get more information about the catalyst/solution interface, double-layer capacitance (C_{dl}) calculations were carried out using cyclic voltammetry (CV) to roughly evaluate their effective electrochemical active surface area on Mo₂N-r, Mo–N and P–Mo–N. The CV was tested with a potential range of -0.2 to 0 V vs RHE at different scan rates, and the Δj at -0.1 V vs scan rate was plotted. The slope was supposed to be twice that of the C_{dl} ^{44,60}. Our results (Supplementary Figure 20) reveal a considerably larger C_{dl} of the P–Mo–N sample (275 mF cm^{-2}) compared with bare Mo–N (115 mF cm^{-2}) and the referenced Mo₂N-r (60 mF cm^{-2}), indicating more accessible electroactive sites created by P doping in the Mo₂N network. The P doping was achieved by BP loading first and then calcination, thus more P element was confined into the surface lattice, which may contribute to the small carrier migration resistance across the catalyst/solution interface and a large C_{dl} .

Moreover, the operating stability of the catalyst is of great concern in the real industrial application. The polarization curve after 10,000 cycles was performed on P–Mo–N catalyst in the 0.5 M H₂SO₄ solution. As given in Fig. 3e, negligible change can be found before and after the continuous cycle test. The chronoamperometry ($j-t$) response was further carried out under three potentials of 145, 157, and 164 mV. The j responses with the corresponding values of 50, 100, and 150 mA/cm² give no obvious decrease or increase during the continuous 12 h measurement (Fig. 3f). The EIS spectrum and XRD pattern of the P–Mo–N catalyst were further tested as given in Supplementary Figure 21. No change to the resistance and phase can be found, further suggesting a good stability of P–Mo–N catalyst. Supplementary Figure 22 gives the contrastive HRTEM images with no change. Moreover, the electrocatalytic HER activity after 3 months (storing in a sample tube without vacuum treatment) was also conducted. Almost no shift of polarization curves after one and three months (Supplementary Figure 23). The effect of P content for HER performance was verified. As given in Supplementary Figure 24a, the 9.5 wt%, 10 wt%, and 10.5 wt% sample show the similar XRD pattern, confirming that the P content in these three values does not change the phase of Mo₂N. The HER activity in Supplementary Figure 24b confirms that the 10 wt.% P doping can induce the best electrocatalytic performance.

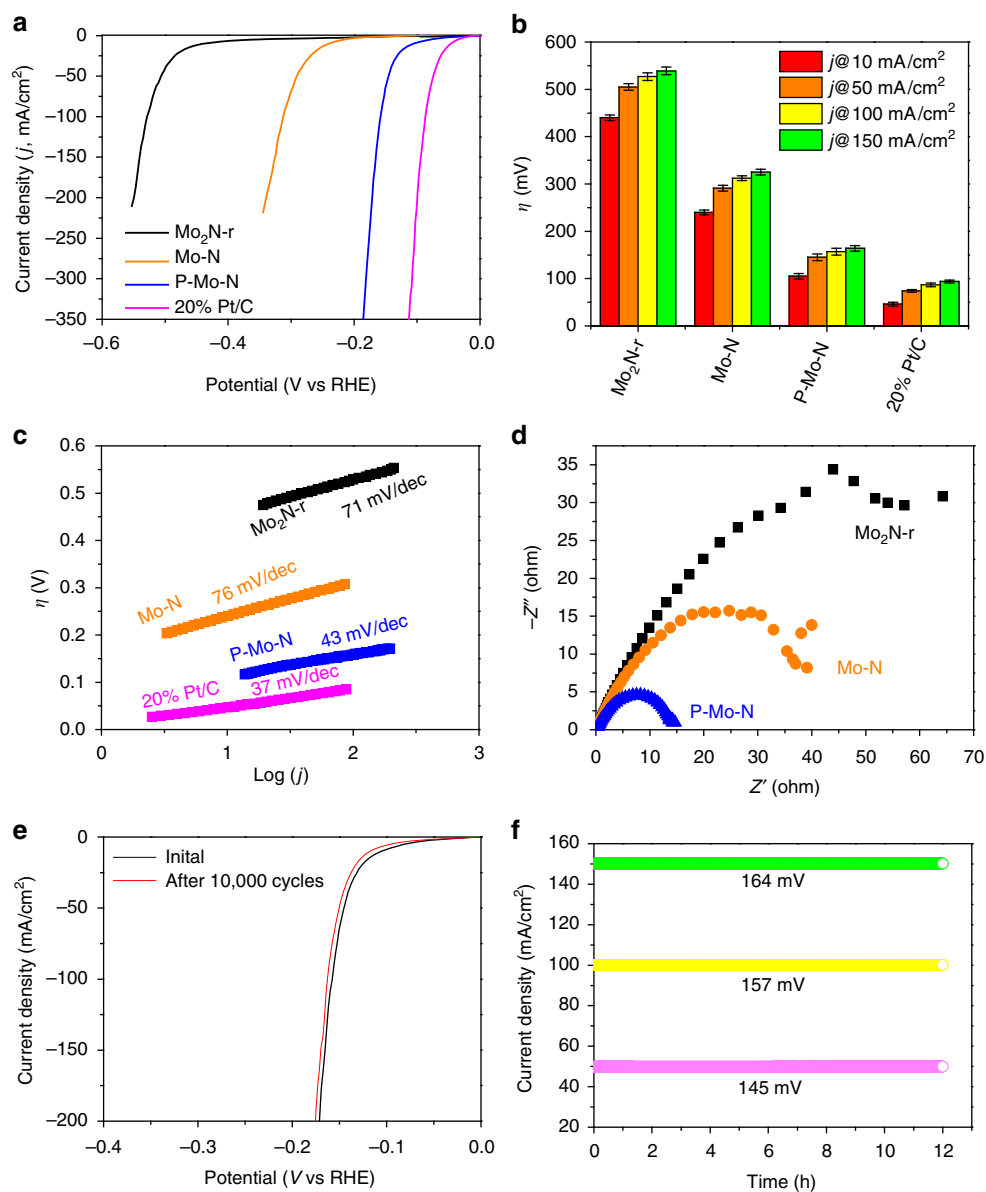


Fig. 3 HER electrocatalysis of $\text{Mo}_2\text{N-r}$, Mo-N , P-Mo-N and reference 20% Pt/C . **a** Polarization curves recorded on glassy carbon electrodes, the catalyst loading was 0.2 mg/cm^2 . **b** The corresponding overpotentials of the samples under the current density (j) values of 10, 50, 100, and 150 mA/cm^2 . Please note that every sample was tested 10 times and then the corresponding standard deviation value was used for the error bar. **c** The Tafel plots, derive from the polarization curves. **d** The electrochemical impedance spectra (EIS) of $\text{Mo}_2\text{N-r}$, Mo-N , and P-Mo-N samples. **e** Durability test of the P-Mo-N catalyst, showing the results of initial and 10,000 cycles. **f** The current density vs time response results under three potentials of 145, 157, and 164 mV . $0.5 \text{ M H}_2\text{SO}_4$ was used as the electrolyte, Ag/AgCl (saturated KCl) and a graphite rod were used as the reference and counter electrodes, respectively

HER mechanism of P-Mo-N. It is found that the as-prepared Mo_2N , P-Mo-N with 10 wt% P, catalyst owns numerous exposed crystal faces, which could reduce its activity in air and lower the Mo-H bonds. This is proven to effectively catalyze water splitting for H_2 production whose performance is superior over most of state-of-art catalysts reported in the literature^{25,37,41}. Furthermore, the P element doping boosts the HER performance greatly and the enhancement should be clarified. In realistic water electrocatalysis, two vital parameters, i.e. interfacial property of catalyst/solution and the intrinsic nature of the catalyst, determine the final performance^{18,21,37,61}. Thus, the interface properties were firstly studied to investigate the improvement shown by P doping. Four solutions with different pH values were chosen for this purpose.

As shown in Fig. 4a, the polarization curves of the P-Mo-N sample in the four varying pH solutions present different

patterns. Typically, in the $0.5 \text{ M H}_2\text{SO}_4$ media ($\text{pH} \sim 0$), the catalyst exhibits the best electrocatalytic performance, followed by that in $0.05 \text{ M H}_2\text{SO}_4$ ($\text{pH} \sim 1$), $0.5 \text{ M Na}_2\text{SO}_4$ ($\text{pH} \sim 6.8$) and 0.1 mM NaOH ($\text{pH} \sim 10$), suggesting that more free H^+ can help obtain a high H_2 evolution performance. Moreover, at the current density of 10 mA/cm^2 , we measured the corresponding potential values: 135, 128, and 100 mV for 0.1 mM NaOH , $0.5 \text{ M Na}_2\text{SO}_4$, and $0.05 \text{ M H}_2\text{SO}_4$, respectively. There is a double electrode layer (DEL) at the solid|liquid interface, this can be attributed to different H^+ concentrations will inducing a varied H^+ adsorption or arrangement⁶². The 0.1 mM NaOH condition for P-Mo-N HER presented in Fig. 4a demonstrated a better performance than bare Mo_2N in $0.5 \text{ M H}_2\text{SO}_4$ (Fig. 3a), suggesting the P doping can induce a favorable H^+ arrangement for HER in the DEL even in a low H^+ concentration solution. The corresponding EIS spectrum

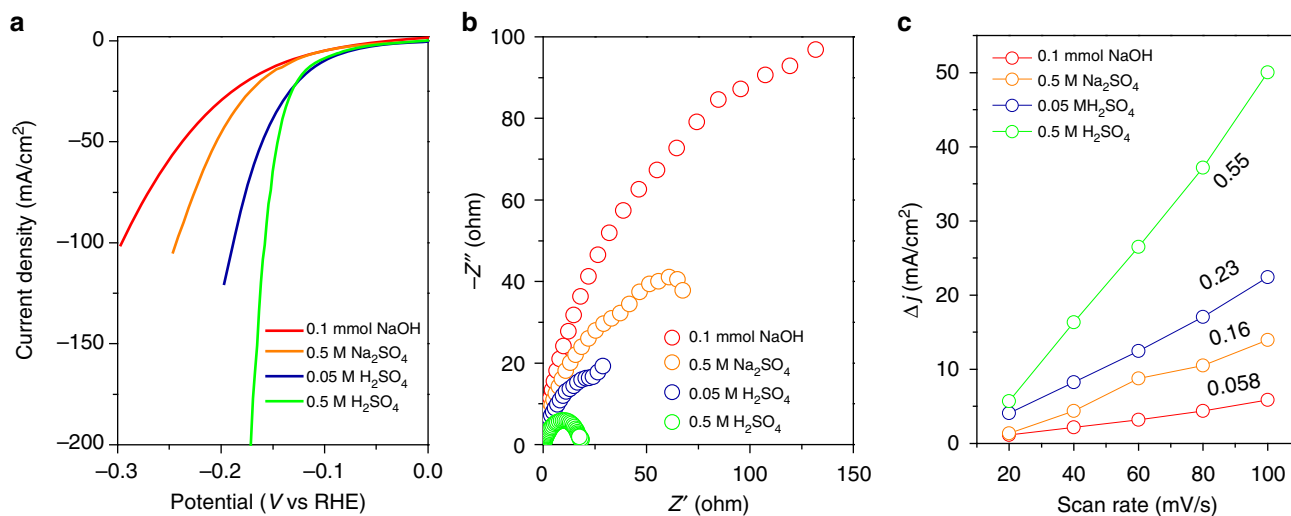


Fig. 4 Water electrolysis in different pH solutions. **a** HER electrocatalysis on P-Mo-N catalyst in the different pH solutions: 0.1 mM NaOH, 0.5 M Na₂SO₄, 0.05 M H₂SO₄, and 0.5 M H₂SO₄; **b** the electrochemical impedance spectra (EIS) of P-Mo-N sample under the four solution: 0.1 mM NaOH, 0.5 M Na₂SO₄, 0.05 M H₂SO₄, and 0.5 M H₂SO₄, the bias voltage is set to be -100 mV; **c** the plots of Δj at -0.1 V vs. RHE against the scan rate, the corresponding slopes are also shown, the corresponding CV curves in the region of -0.2 - 0.0 V vs. RHE are given in Supplementary Figure 24. Please note that the dates of 0.5 M H₂SO₄ condition are obtained from above results, not the new dates

in Fig. 4b in different pH solutions shows that similar trends can be found. For studying the adsorption behavior of reaction species in the DEL, a bias potential of -100 mV (after this potential, the H₂ evolution will start⁶²) was used according to the polarization curves. Supplementary Table 5 shows the corresponding fitted resistance values based on the fitting circuit (Supplementary Figure 19b). Obviously, the R_{ct} in the 0.5 M H₂SO₄ solution gives the smallest value, and it increases with the elevated pH, suggesting that more free H⁺ in the electrolyte will be suitable for DEL formation with a low resistance. The EIS spectrum of bare Mo₂N catalyst was also conducted under the same condition with an R_{ct} value of 62.3 ohm, further confirming that the P doping can induce a suitable H⁺ adsorption and then a low resistance DEL. To get more information about the DEL, the electrocatalytic reaction area was further carried out according to the CV curves under the potential range of -0.2 to 0 V as shown in Supplementary Figure 25. The C_{dl} values were calculated to be 275, 115, 80, and 29 mF/cm² for 0.5 M H₂SO₄, 0.05 M H₂SO₄, 0.5 M Na₂SO₄, and 0.1 mM NaOH, respectively, further validating the above results, that is, more free H⁺ can be adsorbed by the P doped surface of Mo₂N.

The intrinsic nature of the P doped Mo₂N was next investigated for understanding the HER enhancement. Density functional theory (DFT) calculations were carried out. Owing to the more exposed facets of the synthesized Mo₂N sample, four main crystal face models, (112), (200), (220), and (312) with the N replaced by P were established as shown in Supplementary Figure 26 and Fig. 5a-b. For studying the reaction centers, the elements for proton adsorption were also labeled (Supplementary Figure 26). The computational H adsorption free energy values on different reaction centers in different surfaces of the bare Mo₂N and P doped Mo₂N samples are summarized as given in Supplementary Table 6-7 and Fig. 5c. Typically, for the undoped sample, the (200) facet gives a good H adsorption result either on exposed N center or Mo center. However, the Mo atoms in (200) surface can be oxidized easily and then the bare Mo₂N always gives a low HER performance (Fig. 3a). Exposing more facets with lots of grain boundaries can stabilize (200) facet and induce more reaction sites, and then the Mo₂N sample with a grain boundary displays a better HER performance than the one with a single exposed surface. For the P doped sample, the P sites in two

facets of (112) and (312) give suitable HER reaction sites with the relative small H adsorption free energy values of 0.04 and 0.08 eV, respectively. Figure 5c clearly shows that the hydrogen adsorption free energy ($G^*(H)$) gives a very small $G^*(H)$ value for the P-Mo-N sample at P sites, whereas the Mo sites or N sites in doped or bare samples show the strong water adsorption ability and consequent a weak desorption behavior. Supplementary Figure 27 and Fig. 5d, e give the contrastive N-p, P-p and Mo-d orbital density of states (DOS) in four facets of bare and doped Mo₂N samples. Obviously, the p orbitals of P atom in all conditions show a right shift compared to N atoms, suggesting that the more anti-bonding orbital of the P atom will hybridize with the s orbital of the H atom, and then weaken the $G^*(H)$ value. Meanwhile, for the Mo atom, an opposite tendency can be found, further confirming that the P doping is good for the HER process. Moreover, the work functions (W_f) based on ultraviolet-photoelectron spectra (UPS) in Fig. 5f and Supplementary Figure 28 were calculated to be 4.8 and 4.53 eV for Mo₂N and P-Mo₂N, respectively. Note that a small W_f of a catalyst will be helpful for electrons migrating through the sample and then assist with a better activity. Here a low W_f further confirms that the P doping can promote electron transfer and enhance chemical activity.

Discussion

We describe here an air-stable Mo₂N electrocatalyst prepared from a violent solid-state reaction of ethanediamine and MoO₃ by utilizing the strategy discussed above. Owing to the several reaction sites, the Mo₂N was achieved with several exposed crystal facets, which lower the active Mo atom number. Moreover, the by-product of abundant crystal boundaries was beneficial to the HER performance. BP was used for P doping and the obtained P-Mo-N showed an enhanced HER activity compared with bare Mo₂N. Experimental and computational results collectively confirmed more reaction sites provided by P doping, a lower carriers/protons migration resistance across the catalyst/solution interface, as well as a suitable hydrogen adsorption free energy. Such a method for ensuring uniform multi-site solid-state reaction can be extended to synthesis of other materials, and thus enrich earth-abundant elements based catalysts with satisfactory activity. Moreover, the P doping strategy can help us understand more

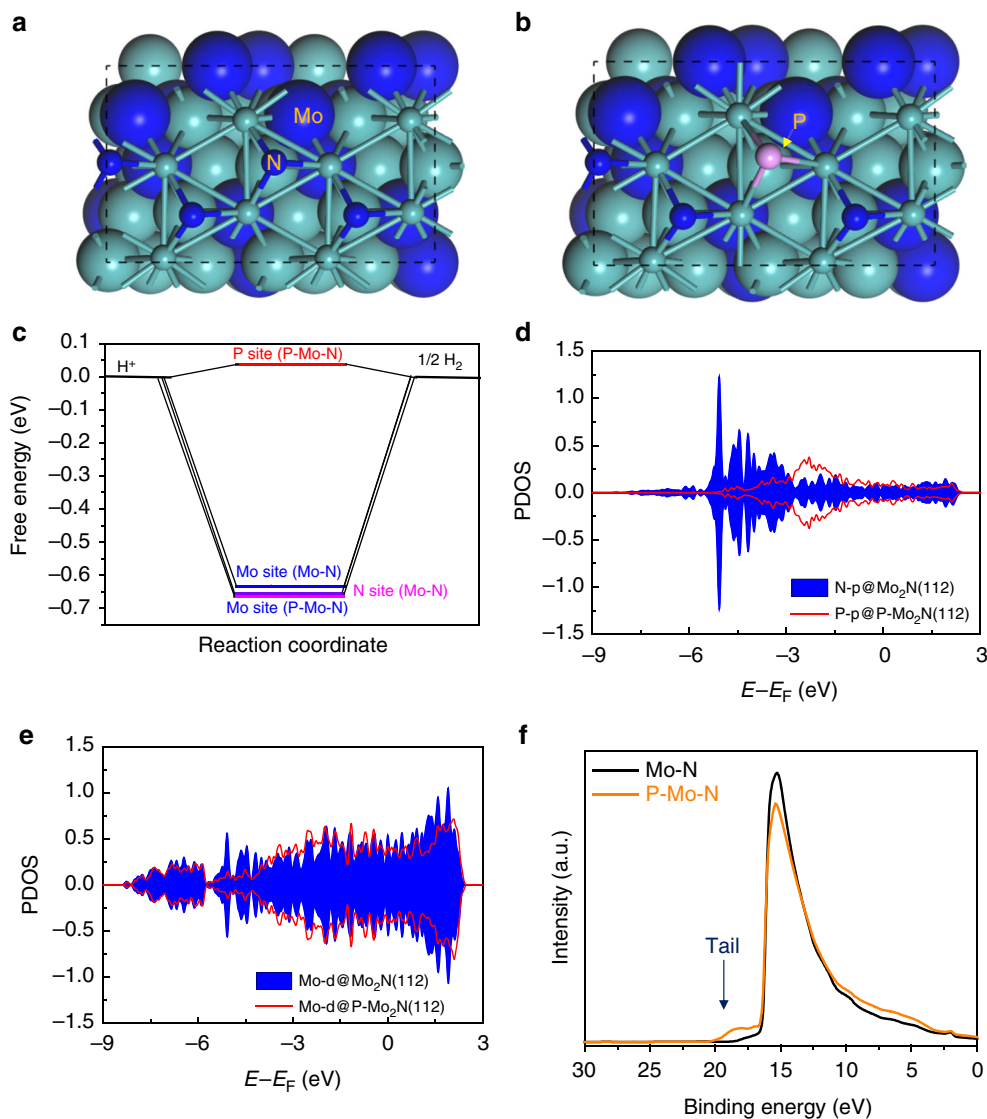


Fig. 5 Electronic structure of Mo₂N and P-Mo₂N. DFT calculation: **a** model of bare Mo₂N (112) facet; **b** model of P doped Mo₂N (112) surface, one N atom was replaced by one P atom; the blue, cyan, and pink spheres are Mo, N, and P atoms, respectively. The dotted gray box in **a** or **b** is the framework of the model. **c** Free energy diagrams for hydrogen adsorption at different sites (Mo, N, and P) on the (112) surface of bare Mo₂N and P doped Mo₂N; computational densities of states (DOS) of **(d)** N-p orbital in bare Mo₂N (112) surface, P-p orbital in P doped Mo₂N (112) surface and **e** Mo-d orbital in bare and doped Mo₂N (112) surface. **f** Ultraviolet-photoelectron spectra of Mo₂N and P doped Mo₂N samples. For the sample of P doped Mo₂N, a tail can be found as depicted by the blue arrow

about electrocatalytic reaction mechanisms such as HER presented here and also design more doped samples to enhance active site exposure and provide more adsorption and desorption characteristics.

Methods

Synthesis of Mo-N. In a typical synthesis, 0.5 g MoO₃ and a certain amount of ethanediamine was first mixed and grinded by a quartz mortar, after that, the mixture was moved to a ball mill and further treated thoroughly for 45 min. Then, the uniform mixture was transferred into one vacuum tube furnace and calcinated under 500 °C for 4 h in a flowing N₂-gas atmosphere. After naturally cooling to room temperature, the product was collected and stored for further use. Please note that without the treatment of the ball mill, an active Mo₂N will be generated.

Synthesis of P-Mo-N. In a typical synthesis, 0.3 g of Mo-N was added into 100 mL BP solution, the mixture was then placed under vacuum and then stirred for 3 h to achieve complete adsorption. After that, the product was treated by centrifugation and vacuum drying. The obtained powder was mixed with ethanediamine by one quartz mortar and then moved into the vacuum tube furnace.

After 4 h 500 °C calcination in a flowing N₂-gas atmosphere, the product was collected, dried at 80 °C and stored for further use.

Material characterization. X-ray diffraction (XRD) patterns of the samples were recorded on a Rigaku Smartlab-9 kW instrument using Cu K α X-ray ($\lambda = 1.54186 \text{ \AA}$) radiation at a scanning rate of 4 °/min in the region of $2\theta = 10\text{--}80^\circ$. X-ray photoelectron spectra (XPS) were acquired on a Kratos Axis Ultra DLD spectrometer with Al K α ($h\nu = 1486.6 \text{ eV}$) as the excitation source. Transmission electron microscopy (TEM) test was performed on a FEI Tecnai G2 F20 electron microscope at an acceleration voltage of 200 kV. Spherical aberration-corrected electron microscope was carried out on a JEM-ARM200F electron microscope (Beijing Zhongkebaice Technology Service Co., Ltd.). The field emission scanning electron microscopy (FESEM) were observed under a SU8020 electron microscopy. Brunauer-Emmett-Teller (BET) surface area analysis was carried out on a Quadrasorb SI-3 equipment.

HER electrode preparation. Typically, 10 mg sample was added into a 50 μL isopropanol, 50 μL nafion (Nafion 117 solution, Sigma-Aldrich) was dispersed into the above solution. The mixture was first fixated and then treated by an oscillator for about 30 min. After that, the mixture was further treated by ultrasound ca. Six

hours to form the uniform ink, which was dropped onto glassy carbon electrodes (5.61 mm diameter, disk area: 0.2475 cm²) with a mass loading of 0.2 mg cm⁻². The prepared electrodes were naturally dried in air.

Electrochemical characterization. All of the electrochemical tests were performed in the room temperature using a typical three-electrode setup. The graphite rod (5.0 mm, 99.997% metals basis) and Ag/AgCl electrodes were used as the counter and reference electrodes, respectively. The electrolyte was 0.5M H₂SO₄ solution. A Zennium Zahner electrochemical workstation was used for the electrocatalytic measurements. Before the test, the as-prepared anodes were activated by a chronopotentiometry scan with the -30 mA cm⁻² current density for 2 h. The Tafel slopes were obtained from the polarization curves by plotting overpotential against log(current density). The steady-state activity was evaluated by chronopotentiometry measurements under different potentials. Please note that the scan rate for the electrocatalytic measurements was 5 mV/s. The C_{dl} was determined by measuring the capacitive current associated with double-layer charging from the scan rate CV-dependence. In our present work, the CV potential window was chosen to be -0.2 to 0 vs Ag/AgCl. The scan rates were 20, 40, 60, 80, and 100 mV s⁻¹. The double-layer capacitance (C_{dl}) was estimated $\Delta j = (j_{\text{charge}} - j_{\text{off charge}})$ at -0.1 V vs Ag/AgCl against the scan rate. The linear slope was twice of the double-layer capacitance C_{dl}. EIS measurements were carried out after the HER tests under the different potentials. The ZSim Demo software was used to fit the EIS results. The measured potentials vs. Ag/AgCl were converted to the reversible hydrogen electrode (RHE) scale according to the following Nernst equation: $E_{\text{RHE}} = E_{\text{Ag/AgCl}} + 0.059 \text{ pH} + E^{\circ}_{\text{Ag/AgCl}}$, where E_{RHE} is the converted potential vs. RHE, $E^{\circ}_{\text{Ag/AgCl}} = 0.1976$ at 25 °C, and $E_{\text{Ag/AgCl}}$ is the experimentally measured potential against Ag/AgCl reference.

Computation model and details. The optimized lattice constants of the Mo₂N unit cell with 4/mmm point group were $a = b = 4.2627 \text{ \AA}$ and $c = 8.0876 \text{ \AA}$. Then four types of five-layered (112), (200), (312), and (220) surface with a 15 Å height were cleaved from their bulk phase and the top three layers were allowed to relax. The single-point energy and the geometry optimization were implemented in the Vinnea ab initio software package (VASP) within the framework of density functional theory⁶³. The exchange-correlation functional adopted the generalized gradient approximation of the Perdew-Burke-Ernzerhof (GGA-PBE) formula⁶⁴. The projector augmented wave method with a cutoff energy of 520 eV was set. The optimization convergence standards were 10⁻⁴ eV for energy and -0.05 eV/Å for force. The formation energy E_f of different surface and P-doping configurations were calculated by:

$$E_f = (E_{\text{total}} - n_{\text{N}}\mu_{\text{N}} - n_{\text{Mo}}\mu_{\text{Mo}} - n_{\text{P}}\mu_{\text{P}})/(n_{\text{N}} + n_{\text{Mo}} + n_{\text{P}}), \quad (1)$$

where the n_{N} , n_{Mo} , and n_{P} were the total number of N, Mo, and P atoms and μ_{N} , μ_{Mo} and μ_{P} were the chemical potential of the element N, Mo, and P defined from the nitrogen gas molecule, bulk Mo metal and black phosphorus phase. E_{total} was the total energy of the configuration. For the adsorption free energy of hydrogen atom, it was calculated based on the formula:

$$G_{*H} = E_{*H} - E_* - 1/2E_{\text{H}_2} + 0.24, \quad (2)$$

where the E_{*H} , E_* , and E_{H_2} were the total energy of the surface with and without hydrogen adsorption and the hydrogen gas molecule. Then 0.24 eV was added to correct the contribution of the zero-point energy and entropy based on previous report⁶⁵.

Data availability

The data that support the findings of this study are available from the corresponding authors upon reasonable request.

Received: 14 August 2018 Accepted: 26 November 2018

Published online: 12 December 2018

References

- Turner, J. A. Sustainable hydrogen production. *Science* **305**, 972–974 (2004).
- Dresselhaus, M. S. & Thomas, I. L. Alternative energy technologies. *Nature* **414**, 332–337 (2001).
- Walter, M. G. et al. Solar water splitting cells. *Chem. Rev.* **110**, 6446–6473 (2010).
- Xu, J. et al. Boosting the hydrogen evolution performance of ruthenium clusters through synergistic coupling with cobalt phosphide. *Energy Environ. Sci.* **11**, 1819–1827 (2018).
- Zhou, H. et al. Water splitting by electrolysis at high current densities under 1.6 volts. *Energy Environ. Sci.* **11**, 2858–2864 (2018).
- Wang, C. et al. Facile synthesis of silk-cocoon S-rich cobalt polysulfide as an efficient catalyst for the hydrogen evolution reaction. *Energy Environ. Sci.* **11**, 2467–2475 (2018).
- Voiry, D. et al. The role of electronic coupling between substrate and 2D MoS₂ nanosheets in electrocatalytic production of hydrogen. *Nat. Mater.* **15**, 1003–1009 (2016).
- Mishra, I. K. et al. Hierarchical CoP/Ni₅P₄/CoP microsheet arrays as a robust pH-universal electrocatalyst for efficient hydrogen generation. *Energy Environ. Sci.* **11**, 2246–2252 (2018).
- Yang, Y. et al. Metal surface and interface energy electrocatalysis: fundamentals, performance engineering, and opportunities. *Chem* **4**, 2054–2083 (2018).
- Laursen, A. B. et al. Climbing the volcano of electrocatalytic activity while avoiding catalyst corrosion: Ni₃P, a hydrogen evolution electrocatalyst stable in both acid and alkali. *ACS Catal.* **8**, 4408–4419 (2018).
- Anantharaj, S. et al. Shrinking the hydrogen overpotential of Cu by 1 V and Imparting ultralow charge transfer resistance for enhanced H₂ evolution. *ACS Catal.* **8**, 5686–5697 (2018).
- Luo, Z. et al. Chemically activating MoS₂ via spontaneous atomic palladium interfacial doping towards efficient hydrogen evolution. *Nat. Commun.* **9**, 2120 (2018).
- Zheng, Y., Jiao, Y., Vasileff, A. & Qiao, S. Z. The hydrogen evolution reaction in alkaline solution: from theory, single crystal models, to practical electrocatalysts. *Angew. Chem. Int. Ed.* **57**, 7568–7579 (2018).
- Wang, Z. L. et al. Spatially confined assembly of monodisperse ruthenium nanoclusters in a hierarchically ordered carbon electrode for efficient hydrogen evolution. *Angew. Chem. Int. Ed.* **57**, 5848–5852 (2018).
- Li, H. et al. Systematic design of superaerophobic nanotube-array electrode comprised of transition-metal sulfides for overall water splitting. *Nat. Commun.* **9**, 2452 (2018).
- Xue, Y. et al. Anchoring zero valence single atoms of nickel and iron on graphdiyne for hydrogen evolution. *Nat. Commun.* **9**, 1460 (2018).
- Xie, L. et al. A Ni(OH)₂-PtO₂ hybrid nanosheet array with ultralow Pt loading toward efficient and durable alkaline hydrogen evolution. *J. Mater. Chem. A* **6**, 1967–1970 (2018).
- Feng, J. X., Wu, J. Q., Tong, Y. X. & Li, G. R. Efficient hydrogen evolution on Cu nanodots-decorated Ni₃S₂ nanotubes by optimizing atomic hydrogen adsorption and desorption. *J. Am. Chem. Soc.* **140**, 610–617 (2018).
- Vincent, I. & Bessarabov, D. Low cost hydrogen production by anion exchange membrane electrolysis: a review. *Renew. Sust. Energy Rev.* **81**, 1690–1704 (2018).
- Gu, Y. et al. Electronic structure tuning in Ni₃FeN/r-GO aerogel toward bifunctional electrocatalyst for overall water splitting. *ACS Nano* **12**, 245–253 (2018).
- Wang, H. et al. Electrochemical tuning of MoS₂ nanoparticles on three-dimensional substrate for efficient hydrogen evolution. *ACS Nano* **8**, 4940–4947 (2014).
- Grönborg, S. S. et al. Visualizing hydrogen-induced reshaping and edge activation in MoS₂ and Co-promoted MoS₂ catalyst clusters. *Nat. Commun.* **9**, 2211 (2018).
- Yin, X. et al. Quasi-emulsion confined synthesis of edge-rich ultrathin MoS₂ nanosheets/graphene hybrid for enhanced hydrogen evolution. *Chem. Eur. J.* **24**, 556–560 (2018).
- Benson, E. E. et al. Balancing the hydrogen evolution reaction, surface energetics, and stability of metallic MoS₂ nanosheets via covalent functionalization. *J. Am. Chem. Soc.* **140**, 441–450 (2018).
- Huang, Y. et al. Nitrogen-doped porous molybdenum carbide and phosphide hybrids on a carbon matrix as highly effective electrocatalysts for the hydrogen evolution reaction. *Adv. Energy Mater.* **8**, 1701601 (2018).
- Jin, Y. et al. Preparation of mesoporous Ni₂P nanobelts with high performance for electrocatalytic hydrogen evolution and supercapacitor. *Int. J. Hydrog. Energy* **43**, 3697–3704 (2018).
- Gong, M. et al. Nanoscale nickel oxide/nickel heterostructures for active hydrogen evolution electrocatalysis. *Nat. Commun.* **5**, 4695 (2014).
- Wang, T., Jin, R., Wu, Y., Zheng, J. & Li, X. Chemical induced fragmentation of MOFs for highly efficient Ni-based hydrogen evolution catalysts. *Nanoscale Horiz.* **3**, 218–225 (2018).
- Wu, Z. et al. Materials chemistry of iron phosphosulfide nanoparticles: synthesis, solid state chemistry, surface structure, and electrocatalysis for the hydrogen evolution reaction. *ACS Catal.* **7**, 4026–4032 (2018).
- Zou, X. et al. In situ generation of bifunctional, efficient Fe-based catalysts from mackinawite iron sulfide for water splitting. *Chem* **4**, 1139–1152 (2018).
- Jiao, Y., Zheng, Y., Davey, K. & Qiao, S. Z. Activity origin and catalyst design principles for electrocatalytic hydrogen evolution on heteroatom-doped grapheme. *Nat. Energy* **1**, 16130 (2016).
- Conway, B. E. & Tilak, B. V. Interfacial processes involving electrocatalytic evolution and oxidation of H₂, and the role of chemisorbed H. *Electrochim. Acta* **47**, 3571–3594 (2002).

33. Li, Y. et al. MoS₂ nanoparticles grown on graphene: an advanced catalyst for the hydrogen evolution reaction. *J. Am. Chem. Soc.* **133**, 7296–7299 (2011).
34. Jaramillo, T. F. et al. Identification of active edge sites for electrochemical H₂ evolution from MoS₂ nanocatalysts. *Science* **317**, 100–102 (2007).
35. Lv, C. et al. Ultrafast synthesis of molybdenum carbide nanoparticles for efficient hydrogen generation. *J. Mater. Chem. A* **5**, 22805–22812 (2017).
36. Wu, Z. et al. MoS₂–MoP heterostructured nanosheets on polymer-derived carbon as an electrocatalyst for hydrogen evolution reaction. *J. Mater. Chem. A* **6**, 616–622 (2018).
37. Yan, H. et al. Holey reduced graphene oxide coupled with an Mo₂N–Mo₂C heterojunction for efficient hydrogen evolution. *Adv. Mater.* **30**, 1704156 (2018).
38. Zhang, X. et al. Molybdenum phosphide/carbon nanotube hybrids as pH-universal electrocatalysts for hydrogen evolution reaction. *Adv. Funct. Mater.* **28**, 1706523 (2018).
39. Lv, Z. et al. Well-dispersed molybdenum nitrides on a nitrogen-doped carbon matrix for highly efficient hydrogen evolution in alkaline media. *J. Mater. Chem. A* **5**, 20932–20937 (2017).
40. Chen, Y.-Y. et al. Pomegranate-like N, P-doped Mo₂C@C nanospheres as highly active electrocatalysts for alkaline hydrogen evolution. *ACS Nano* **10**, 8851–8860 (2016).
41. Ma, L., Ting, L. R. L., Molinari, V., Giordano, C. & Yeo, B. S. Efficient hydrogen evolution reaction catalyzed by molybdenum carbide and molybdenum nitride nanocatalysts synthesized via the urea glass route. *J. Mater. Chem. A* **3**, 8361–8368 (2015).
42. Sun, Y. et al. Strong electronic interaction in dual-cation-incorporated NiSe₂ nanosheets with lattice distortion for highly efficient overall water splitting. *Adv. Mater.* **30**, 1802121 (2018).
43. Anjum, M. A. R. & Lee, J. S. Sulfur and nitrogen dual-doped molybdenum phosphide nanocrystallites as an active and stable hydrogen evolution reaction electrocatalyst in acidic and alkaline media. *ACS Catal.* **7**, 3030–3038 (2017).
44. Wu, Y. et al. Electron density modulation of NiCo₂S₄ nanowires by nitrogen incorporation for highly efficient hydrogen evolution catalysis. *Nat. Commun.* **9**, 1425 (2018).
45. Guan, C. et al. Hollow Mo-doped CoP nanoarrays for efficient overall water splitting. *Nano Energy* **48**, 73–80 (2018).
46. Wei, H. et al. Molybdenum carbide nanoparticles coated into the graphene wrapping N-doped porous carbon microspheres for highly efficient electrocatalytic hydrogen evolution both in acidic and alkaline media. *Adv. Sci.* **5**, 1700733 (2018).
47. Wang, J., Wei, Z., Mao, S., Li, H. & Wang, Y. Highly uniform Ru nanoparticles over N-doped carbon: pH and temperature-universal hydrogen release from water reduction. *Energy Environ. Sci.* **11**, 800–806 (2018).
48. Ji, L. et al. N, P-doped molybdenum carbide nanofibers for efficient hydrogen production. *ACS Appl. Mater. Interfaces* **10**, 14632–14640 (2018).
49. Zhang, J. et al. Facile one-step synthesis of phosphorus-doped CoS₂ as efficient electrocatalyst for hydrogen evolution reaction. *Electrochim. Acta* **259**, 955–961 (2018).
50. Gu, H., Fan, W. & Liu, T. Phosphorus-doped NiCo₂S₄ nanocrystals grown on electrospun carbon nanofibers as ultra-efficient electrocatalysts for the hydrogen evolution reaction. *Nanoscale Horiz.* **2**, 277–283 (2017).
51. Shi, Z. et al. Phosphorus–Mo₂C@carbon nanowires toward efficient electrochemical hydrogen evolution: composition, structural and electronic regulation. *Energy Environ. Sci.* **10**, 1262–1271 (2017).
52. Sun, A., Shen, Y., Wu, Z. & Wang, D. N-doped MoP nanoparticles for improved hydrogen evolution. *Int. J. Hydrog. Energy* **42**, 14566–14571 (2017).
53. Xie, J. et al. Controllable disorder engineering in oxygen-incorporated MoS₂ ultrathin nanosheets for efficient hydrogen evolution. *J. Am. Chem. Soc.* **135**, 17881–17888 (2013).
54. Li, G. et al. All the catalytic active sites of MoS₂ for hydrogen evolution. *J. Am. Chem. Soc.* **138**, 16632–16638 (2016).
55. Xie, J. et al. Defect-rich MoS₂ ultrathin nanosheets with additional active edge sites for enhanced electrocatalytic hydrogen evolution. *Adv. Mater.* **25**, 5807–5813 (2013).
56. Kong, L. et al. g-C₃N₄ Loading black phosphorus quantum dot for efficient and stable photocatalytic H₂ generation under visible light. *Adv. Funct. Mater.* **28**, 1800668 (2018).
57. Yan, J. et al. Black phosphorus-based compound with few layers for photocatalytic water oxidation. *ChemCatChem* **10**, 3424–3428 (2018).
58. Yan, J. et al. Nitrogen promoted molybdenum dioxide nanosheets for electrochemical hydrogen generation. *J. Mater. Chem. A* **6**, 12532–12540 (2018).
59. Xiao, P. et al. Molybdenum phosphide as an efficient electrocatalyst for the hydrogen evolution reaction. *Energy Environ. Sci.* **7**, 2624–2629 (2014).
60. Yue, Q. et al. MoP is a novel, noble-metal-free cocatalyst for enhanced photocatalytic hydrogen production from water under visible light. *J. Mater. Chem. A* **3**, 16941–16947 (2015).
61. Yan, J. et al. Fe (III) doped NiS₂ nanosheet: a highly efficient and low-cost hydrogen evolution catalyst. *J. Mater. Chem. A* **5**, 10173–10181 (2017).
62. Ledezma-Yanez, I. et al. Interfacial water reorganization as a pH-dependent descriptor of the hydrogen evolution rate on platinum electrodes. *Nat. Energy* **2**, 17031 (2017).
63. Kresse, G. & Furthmüller, J. Efficient iterative schemes for ab initio total-energy calculations using a plane-wave basis set. *Phys. Rev. B: Condens. Matter Mater. Phys.* **54**, 11169–11186 (1996).
64. Monkhorst, H. J. & Pack, J. D. Special points for Brillouin-zone integrations. *Phys. Rev. B* **13**, 5188–5192 (1976).
65. Tang, Q. & Jiang, D. Mechanism of hydrogen evolution reaction on 1T-MoS₂ from first principles. *ACS Catal.* **6**, 4953–4961 (2016).

Acknowledgements

We thank the support from the National Key Research Program of China (2017YFA0204800, 2016YFA0202403), Natural Science Foundation of China (No. 21603136, 91733301), the National Science Basic Research Plan in Shaanxi Province of China (2017JM2007), the Changjiang Scholar and Innovative Research Team (IRT_14R33), the 111 Project (B14041), the Fundamental Research Funds for the Central Universities (GK201602007, 2018CSLZ011), and the Chinese National 1000-Talent-Plan program are also acknowledged. T.Y.M. acknowledges the support from Australian Research Council (ARC) through Discovery Early Career Researcher Award (DE150101306) and Linkage Project (LP160100927).

Author contributions

J.Y. and T.M. conceived and designed the experiments. J.Y., L.K., J.W., and X.H. carried out material synthesis, performed physical, and chemical characterization, and conducted the electrochemical measurements. J.Y., T.M., S.L., and S.-T.L. performed data analysis. Y.J. and Y.L. performed all the DFT calculations. All authors discussed the results and co-wrote the paper.

Additional information

Supplementary information accompanies this paper at <https://doi.org/10.1038/s42004-018-0097-9>.

Competing interests: The authors declare no competing interests.

Reprints and permission information is available online at <http://npg.nature.com/reprintsandpermissions/>

Publisher's note: Springer Nature remains neutral with regard to jurisdictional claims in published maps and institutional affiliations.



Open Access This article is licensed under a Creative Commons Attribution 4.0 International License, which permits use, sharing, adaptation, distribution and reproduction in any medium or format, as long as you give appropriate credit to the original author(s) and the source, provide a link to the Creative Commons license, and indicate if changes were made. The images or other third party material in this article are included in the article's Creative Commons license, unless indicated otherwise in a credit line to the material. If material is not included in the article's Creative Commons license and your intended use is not permitted by statutory regulation or exceeds the permitted use, you will need to obtain permission directly from the copyright holder. To view a copy of this license, visit <http://creativecommons.org/licenses/by/4.0/>.

© The Author(s) 2018